DEVELOPMENT OF AN AUTOMATED ARCTIC CLOUD MASK USING CLEAR-SKY SATELLITE OBSERVATIONSTAKEN OVER THE SHEBA and ARM NSA SITES

D.A. Spangenberg, V. Chakrapani, and D.R. Doelling
Analytical Services and Materials, Inc., Hampton, Virginia

P. Minnis
Atmospheric Sciences, NASA-Langley Research Center, Hampton, Virginia

R.F. Arduini
SAIC Inc., Hampton Virginia

DEVELOPMENT OF AN AUTOMATED ARCTIC CLOUD MASK USING CLEAR-SKY SATELLITE OBSERVATIONSTAKEN OVER THE SHEBA and ARM NSA SITES

D.A. Spangenberg, V. Chakrapani, and D.R. Doelling
Analytical Services and Materials, Inc., Hampton, Virginia

P. Minnis
Atmospheric Sciences, NASA-Langley Research Center, Hampton, Virginia

R.F. Arduini
SAIC Inc., Hampton Virginia

1. INTRODUCTION

Detecting clouds with satellite data in polar regions is difficult due to minimal contrast between clouds and the underlying snow surface in visible (VIS; 0.65μm) wavelengths. The infrared (IR; 11μm) band often shows that the surface is at the same temperature or even colder than clouds, further complicating cloud detection. Also, the boundary layer can have large areas of haze, thin fog, or diamond dust that are not seen in either VIS or IR imagery. Minnis et al. (2001) used a subjective cloud mask that exploits the brightness temperature difference (BTD_{34}) between the 3.7- (channel-3) and 10.8-μm (channel-4) bands of NOAA 12 and 14 Advanced Very High Resolution (AVHRR) data to detect clouds. BTD_{34} can discriminate clouds over snow and ice surfaces because 3.7-μm albedo of snow is small compared to that of clouds. Except for the use of a theoretical model based radiative transfer computations assuming a spherical ice crystal for snow (Han et al. 1999), detection methods have relied on empirical, subjectively determined criteria for detecting clouds with 3.7-μm data (e.g., Allen et al. 1990). Accurate knowledge of snow reflectance R_{37} at 3.7 μm is essential for improved automation of cloud detection algorithms over snow surfaces during daytime. To achieve such improvements, it is necessary to model the angular dependence of R_{37}. In this paper, a bidirectional reflectance function (BRDF) is derived using a hexagonally shaped crystal to simulate snow grains. The model-predicted reflectances are compared observed reflectances over clear snow using the AVHRR R_{37} measurements of Minnis et al. (2001) taken during May 1998. These observations were coincident with data taken at the surface over the Surface Heat Budget of the Arctic Ocean (SHEBA) site in the polar ice cap. These and other surface observations are used to help explain the observed differences and to ensure that the skies were cloud free.

Corresponding Author Address: D. A. Spangenberg, AS&M, Inc., Hampton, VA 23666; e-mail: d.a.spangenberg@larc.nasa.gov.

2. DATA

For this study, all NOAA-12 and 14 orbits that encompass the Atmospheric Radiation Measurement (ARM) North Slope of Alaska (NSA) site at Barrow, AK and the SHEBA site are used to develop a May-July 1998 clear-sky dataset, using the method of Minnis et al. (2001). The 1-km pixel data were averaged on a 56 x 56 km^2 regional grid.

3. 3.7 μm SNOW REFLECTANCE

The clear-sky solar portion of the AVHRR 3.7μm band was extracted from the total radiance using the method of Allen et al. (1989). The 11μm brightness temperature T_4 is used in the Planck function at 3.7μm B_{37} to estimate the infrared portion at 3.7μm. The reflected solar component is

$$R_{37} = [\varepsilon_{37}{}^*B_{37}(T_3) - \varepsilon_{37}{}^*B_{37}(T_4)] / [(\mu_0{}^*S_{37}) - \varepsilon_{37}{}^*B_{37}(T_4)] \quad (1)$$

where T_3 is the 3.7-μm brightness temperature, μ_0 is the cosine of the solar zenith angle, and S_{37} is the solar constant at 3.7 μm (3.47 Wm^{-2}μm^{-1}). A value of 0.964 was used for clear snow emittance ε_{37}. Its value was determined as noted by Trepte et al. (1999).. Typical clear-sky values of R_{37} over snow range from 0.0 to 0.02, while clouds have values ranging from 0.04 to 0.40 depending on optical depth τ and effective droplet size r_e. The quantities in (1) all refer to the top of the atmosphere so that the emissivities and reflectances include both surface and atmospheric effects.

Theoretical reflectance models at 3.7 μm were developed from calculations using an adding-doubling radiative transfer model developed by Minnis, et al. (1993). The snow surface was approximated using an optically thick (τ=1000) layer made up of randomly oriented, hexagonal ice crystals having a length to width ratio L/D of 750μm/160μm. The optical properties of the ice crystals, including the scattering phase function, are from Takano and Liou (1989). The model BRDFs at the top of the atmosphere were computed using a radiative transfer model incorporating the May 22 (clear-sky) arctic atmosphere from the European Center for Medium-Range Weather Forecasting analysis and a correlated-k distribution method (Kratz 1995).
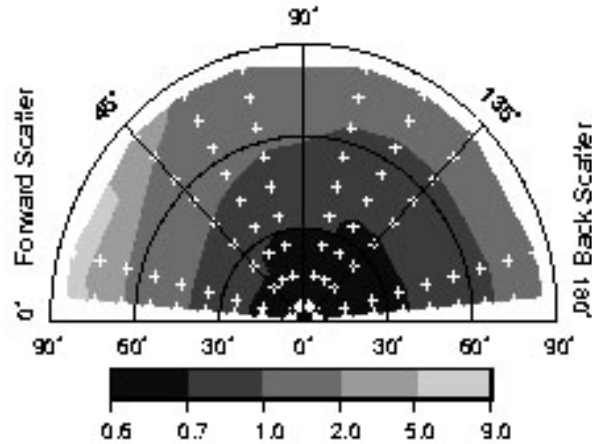
Figure 1. Theoretical 3.7-µm reflectance factors for SZA = 65°. Lower axis is VZA (0-90). Polar axis is RAA.

Figure 1 shows the normalized BRDF over snow as a function of satellite view geometry for a solar zenith angle SZA of 65°. The values of R_{37} were divided by the albedo (integral of R_{37}) to obtain these normalized values. Forward scatter is in the 0-90° relative azimuth RAZ range. For small viewing zenith angles VZA between 0 and 30°, the reflectance is about 60-80% of the albedo, ranging to as much as 4 times greater than the albedo for forward scatter at large VZAs.

For comparison with the models, the observed clear-sky values of R_{37} were averaged in VZA bins for both forward and backscattering conditions for different overpass time intervals. To minimize the effects of striping and cloud shadows in the data, only the clear-sky values from grid boxes having cloud amounts less than 10% were used. For each clear observation, a model reflectance was computed based on the viewing geometry. Since the model and observations may not have matching reflectivities, an offset ratio was computed as the mean of the satellite reflectance divided by the mean model R_{37} for each of the 4 bins. This approach time binning groups together points having similar sun-satellite and view geometries, and similar orbit orientations

4.0 RESULTS

Table 1 summarizes the results for the two pairs of UTC and RAA bins. The ratios for the NOAA-12 data range from 0.7-0.8, indicating the model is overestimating the satellite observations by 20-30%. The NOAA-14 ratios show better agreement except for the 21-01 GMT, 90° to 180° azimuth bin where a ratio of 0.81 is observed. The viewing geometries for the NOAA-12 AVHRR observations did not differ significantly from those for NOAA-14 suggesting that there are some relative calibrations differences between channels 3 ad 4 for the two satellites.

A third order polynomial was fit to both the satellite and theoretical model data in each of the bins, with the model points having very little scatter about the fit.

NOAA-12

RAA	0 - 5 UTC			16 - 22 UTC		
	Ratio	RMS_O	RMS_M	Ratio	RMS_O	RMS_M
0° to 90°	0.784	1.8E-3 *22.2%*	1.9E-3 *23.1%*	0.713	2.0E-3 *26.3%*	2.0E-3 *27.0%*
90° to 180°	0.764	2.1E-3 *24.4%*	2.3E-3 *27.1%*	0.702	1.8E-3 *23.0%*	1.9E-3 *23.7%*

NOAA-14

RAA	13 - 18 UTC			21 - 01 UTC		
	Ratio	RMS_O	RMS_M	Ratio	RMS_O	RMS_M
0° to 90°	0.994	3.1E-3 *26.5%*	3.2E-3 *27.4%*	1.120	2.7E-3 *22.8%*	2.8E-3 *23.6%*
90° to 180°	1.021	3.0E-3 *24.9%*	3.0E-3 *24.9%*	0.805	2.0E-3 *24.5%*	2.1E-3 *25.4%*

Table 1. Summary of model and observation comparisons of R_{37} for May 1998 AVHRR data.

The model curve was then adjusted to agree with the satellite observations using the offset ratio. Figure 2 shows the resulting curves for the unadjusted model and the observations for NOAA-14 backscatter during the morning (1300-1800 UTC) overpasses. The ratio in this case is 1.02 and the agreement between the two curves is remarkable. The rms differences between the model fits (unadjusted RMS_o and adjusted RMS_m) and the observations were computed for each case. For Fig. 2, both rms differences are ~25%. Scatter in the observations is much greater than that in the models indicating that factors other than angular variations are affecting the observed reflectances. Possible sources include variations in snow grain size and shape, snow purity, ice leads, ice ridges, leads, and cloud contamination

Figure 3 shows the results for the NOAA-12 forward scattering afternoon (00- 05 UTC) data. The theoretical reflectance model shows R_{37} increasing by a factor 1.8 from nadir to 60°, while the mean R_{37} rises dramatically
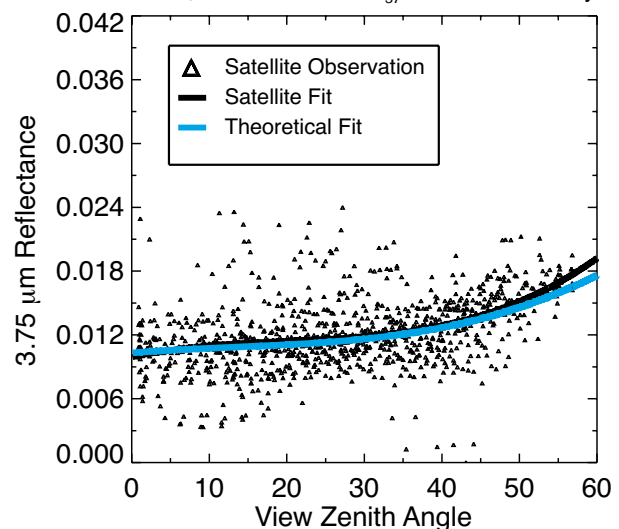

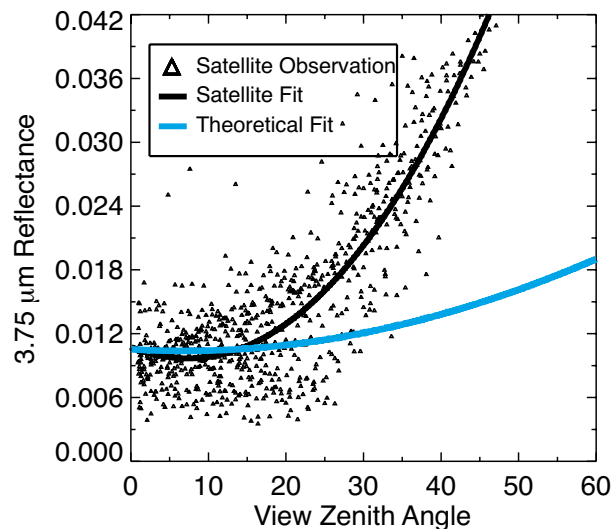Figure 2. May 1998 NOAA-14 R_{37} for 1300 -1800 UTC and 90° < RAA ≤ 180°.

Figure 3. May 1998 NOAA-12 R_{37} for 1300 -1800 UTC and 0° < RAA ≤ 90°.

at VZA = 20° by a factor of 4 at VZA = 45°. The other NOAA-12 forward scattering data also produced a curve similar to that in Fig. 3.

Examination of the imagery for the cases with VZA > 25° in Fig. 3 revealed that the data are from scenes that appear to contain haze. Satellite images suspected of containing haze at 0041 UTC, 24 May are shown in Fig. 4. The VIS image (Fig. 4a) shows a gradual increase in brightness to the right corresponding with increasing VZA in the forward scattering direction, while the IR data (Fig. 4b) indicate the presence of some high clouds on both sides of the image. A large area of apparently clear skies occupies most of the right 2/3 of the images including the SHEBA site. However, the BTD_{34} and BTD_{45} images (Figs. 4c and d) reveal some structure that is not apparent in the other two images. Just west of SHEBA, both BTD_{34} and BTD_{45} increase significantly. These increases correspond to the rapid rise in R_{37} seen in Fig. 3. This feature is consistent with an optically thin cloud or haze layer. A sounding taken from SHEBA at 1121 UTC, 24 May (Fig. 5) shows a strong inversion near the surface with high relative humidity. The SHEBA weather observation report at 1200 UTC indicated fog coincident with clear skies and maximum visibility, suggesting a thin ground-level haze layer. Because surface temperatures were relatively high. the haze would probably not be composed of diamond dust. Using the reflectance models of Minnis et al. (1998), it was found that if it is assumed that the haze comprises water droplets with an effective radius of 4 μm, an optical depth only 0.12 is necessary to explain the differences in Fig. 3. Thus, the 3.7-μm reflectance is extremely sensitive to the presence of haze. Conversely, it clear that this channel is well-suited for detecting clouds over snow.

The haze was also occasionally seen at the SHEBA site during May 24-25. The NOAA Environmental Technology Laboratory DABUL Lidar returns from May 24 (not shown) show some low-level signals between 0600 and 1800 UTC that are likely low-level haze. The increase in incident sunlight during the midday precludes detection of thin aerosol layers near the surface. Also, The pattern of apparent haze seen in Figs. 4a and 4b persisted from May 23-25, during a time of light winds, strong surface inversions, and high surface pressure. Analyses of all of the results showed that the haze was most evident for RAA between 0° and 10°. Arctic haze must be taken into account when modeling clear-sky snow surfaces, since those regions would be classified as cloudy by the theoretical R_{37} model.

5.0 CONCLUSIONS

A theoretical model of snow reflectance was evaluated over northern Alaska and the adjacent Arctic Ocean. The model shows the same trends as the observed 3.7-μm reflectances, but underestimates them for the NOAA-12 satellite. There is much better agreement for NOAA-14. Also, clear-sky arctic haze is the apparent reason for major differences between the model and satellite data for certain viewing geometries.

An automated cloud mask has been developed that incorporates the theoretical snow 3.7-μm reflectance models, but it may need to be updated to include a correction based on the R_{37} observations taken over SHEBA and the ARM NSA. The observed model fit for the haze regimes may be used, instead of the theory, to prevent an over-prediction of clouds in otherwise clear haze areas. A new clear category, Arctic haze, may be included in the output, however, to recognize the variation of Arctic haze. The standard deviation of the $R_{3.7}$ data can be added to the model fit or to the satellite fit in haze regimes to get a clear-cloud threshold based on satellite viewing geometry during daylight hours. Other months will be examined to test the robustness of the May 1998 relationships and to determine if theoretical models can be applied for ocean and bare tundra scenes for the summer (melt) season. It will then be possible to apply the results to other months and years for data similar to those taken by the AVHRR.

5.0 REFERENCES

Allen, R.C., P.A. Durkee, and C.H. Wash, 1990: Snow/cloud discrimination with multispectral satellite measurements. *J. Appl. Meteor.*, **29**, 994-1004.

Han, W., K. Stamnes, and D. Lubin, 1999: Remote sensing of surface and cloud properties in the Arctic from AVHRR measurements. *J. Appl. Meteor.*, **38**, 989-1011.
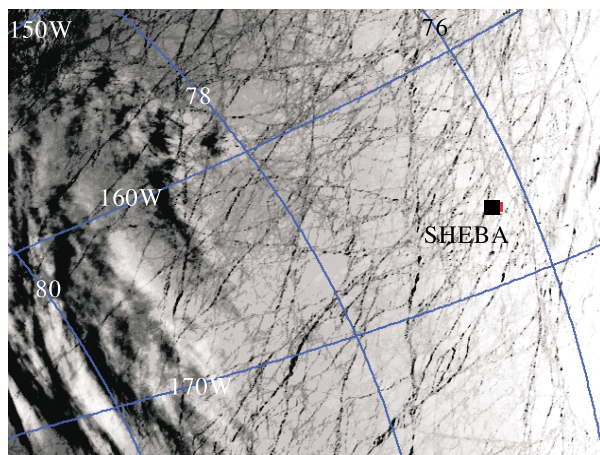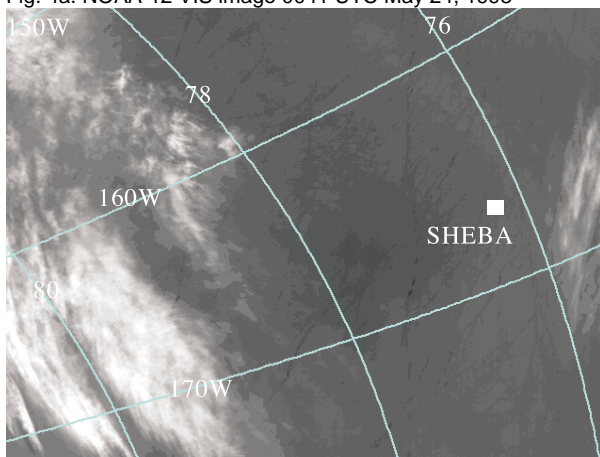
Fig. 4a. NOAA-12 VIS image 0041 UTC May 24, 1998

Fig. 4c. NOAA-12 *BTD*$_{34}$ image 0041 UTC May 24, 1998
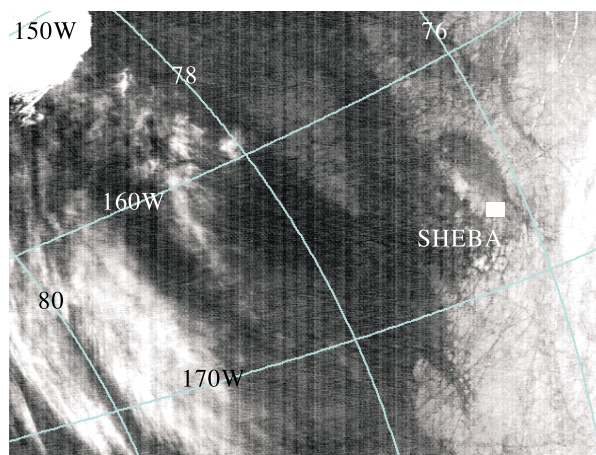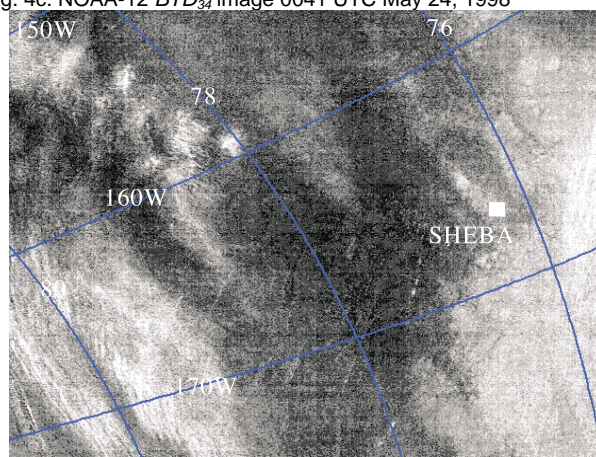

Fig. 4b. NOAA-12 IR image 0041 UTC May 24, 1998

Fig. 4d. NOAA-12 *BTD*$_{45}$ image 0041 UTC May 24, 1998

Kratz, D.P., 1995: The correlated-k distribution technique as applied to the AVHRR channels. *J. Quant. Spectrosc. Radiat. Transfer*, **53**, 501-51.

Minnis, P., Doelling, D.R., V. Chakrapani, D.A. Spangenberg, L. Nguyen, R. Palikonda, T. Uttal, M. Shupe, and R.F. Arduini, 2001: Cloud coverage and height during FIRE ACE derived from AVHRR data. *J. Geophys. Res.*, in press.

Minnis, P., P. W. Heck, and D. F. Young. Inference of cirrus cloud properties from satellite- observed visible and infrared radiances. Part II: Verification of theoretical radiative properties. *J. Atmos. Sci.*, **50**, 1305-1322, 1993.

Minnis, P., D. F. Young, L. Nguyen, D. P. Garber, W. L. Smith, Jr. and R. Palikonda, 1998: Transformation of contrails Into cirrus during SUCCESS. *Geophys. Res. Lett.*, **25**, 1157-1160.

Takano, Y. and K. N. Liou, 1989: Radiative transfer in cirrus clouds: I single scattering and optical properties of oriented hexagonal ice crystals. *J. Atmos. Sci.*, **46**, 3-20.

Trepte, Q., Y. Chen, S. Sun-Mack, P. Minnis, D. F. Young, B. A. Baum, and P. W. Heck, 1999: Scene identification for the CERES cloud analysis subsystem. *Proc. AMS 10th Conf. Atmos. Rad.*, Madison, WI, June 28 – July 2, 169-172.
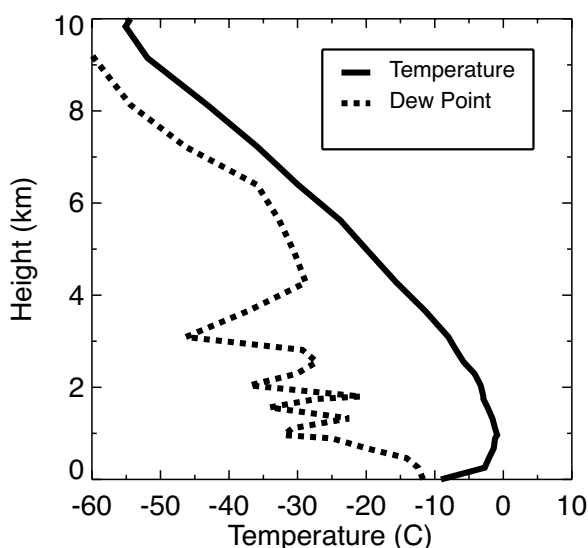
Fig. 5. May 24, 1998 SHEBA sounding at 1121 UTC.